Josephine F. L. Lox, Zhiya Dang, Volodymyr M. Dzhagan, Daniel Spittel, Beatriz Martín-García, Iwan Moreels, Dietrich R. T. Zahn, Vladimir Lesnyak

Near-Infrared Cu–In–Se-Based Colloidal Nanocrystals via Cation Exchange

Erstveröffentlichung in / First published in:

Chemistry of Materials. 2018, 30(8), S. 2483-2858. ACS Publications. ISSN 1520-5002.

DOI: https://doi.org/10.1021/acs.chemmater.7b05187

CHEMISTRY OF MATERIALS
Cite This: Chem. Mater. 2018, 30, 2607−2617
Article
pubs.acs.org/cm

Near-Infrared Cu−In−Se-Based Colloidal Nanocrystals via Cation Exchange

Josephine F. L. Lox,[†,⊥] Zhiya Dang,[‡,⊥] Volodymyr M. Dzhagan,[§,∥] Daniel Spittel,[†] Beatriz Martín-García,[‡] Iwan Moreels,[‡] Dietrich R. T. Zahn,[§] and Vladimir Lesnyak*[,†]

[†]Physical Chemistry, TU Dresden, Bergstrasse 66b, Dresden 01062, Germany
[‡]Department of Nanochemistry, Istituto Italiano di Tecnologia, via Morego, 30, Genova 16163, Italy
[§]Semiconductor Physics, Chemnitz University of Technology, Chemnitz D-09107, Germany
[∥]Institute of Semiconductor Physics, National Academy of Sciences of Ukraine, Kiev 03028, Ukraine

Supporting Information

ABSTRACT: We developed a three-step colloidal synthesis of near-infrared (NIR) active Cu−In−Se (CISe)-based nanocrystals (NCs) via a sequential partial cation exchange realized in one pot. In the first step, binary highly copper deficient $Cu_{2-x}Se$ NCs were synthesized, followed by a partial cation exchange of copper to indium ions, yielding CISe NCs. This reaction allows for a precise control of the composition of the resulting NCs through a simple variation of the ratio between guest-cation precursors and parent NCs. To enhance the stability and the photoluminescence (PL) properties of the NCs, a subsequent ZnS shell was grown in the third step, resulting in CISeS/ZnS core/shell particles. These core/shell hetero-NCs exhibited a dramatic increase in size and a restructuring to trigonal pyramidal shape. The shell growth performed at a relatively high temperature (250 °C) also led to anion exchange, in which sulfur replaced part of selenium atoms close to the surface of the NCs, forming alloyed CISeS core structure. This efficient anion exchange is rarely reported for I−III−VI-based nanomaterials. Furthermore, we demonstrated that at higher reaction temperature, it is possible to obtain In-rich CISeS/ZnS NCs whose emission was shifted to the visible region. Therefore, a careful tuning of the reaction parameters, such as the Cu:Se and Cu:In ratios, temperature, and time, enables a distinct control over the size and composition of the NCs while maintaining their crystal structure. By varying the size of the CISeS/ZnS NCs from 9 to 18 nm, the PL spectra could be tuned, covering a wide NIR range with maxima from 990 to 1210 nm. Thus, in these experiments, we demonstrated a clear dependence of the optical properties of these materials on their size and extended the PL range of CISe-based NCs further to the infrared part of the spectrum. The results obtained might be important not only to elucidation of fundamentals of ion exchange reactions but also may provide a general preparative approach to a wide variety of copper chalcogenide-based NCs with well-controlled size, shape, composition, and even crystal structure.

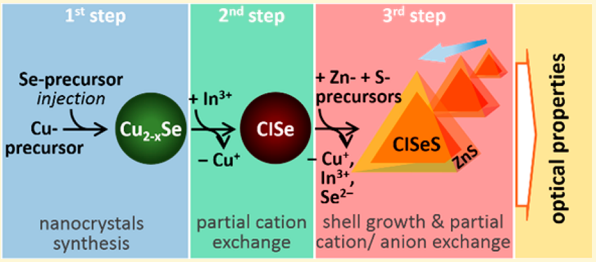

INTRODUCTION

Colloidal semiconductor nanocrystals (NCs) have gained increasing scientific attention due to their unique size- and shape-dependent optoelectronic properties dictated by quantum confinement.[1−3] They hold a huge potential as materials to be employed in optoelectronic devices as well as in the field of biomedicine.[3−5] So far, the study of the semiconductor NCs has mainly focused on binary II−VI, IV−VI, and to some extent on III−V compounds, MX (M^{2+}=Cd^{2+}, Hg^{2+}, Pb^{2+}; M^{3+}=In^{3+}; X^{2-}=S^{2-}, Se^{2-}, Te^{2-}; X^{3-}=P^{3-}), which are particularly promising for optoelectronic and photovoltaic applications.[6−8] Despite their advantages, they contain toxic elements, which can be hazardous when released to the environment. For this reason, their widespread applicability faces serious restrictions. Therefore, in the past decades, the focus of research has broadened out on copper chalcogenide-based ternary and quaternary compounds, e.g. $CuInS(Se)_2$ (CIS(Se)), Cu−Zn−In−S(Se) (CZIS(Se)), and $Cu_2ZnSnS(Se)_4$ (CZTS(Se)), which have proven themselves as outstanding alternatives to the II−VI and IV−VI families of semiconductor nanoparticles.[9−11] An advantage of these materials consists in their low toxicity, giving them permission to widen the range of applications. Especially in vivo imaging of biological processes becomes feasible and is facilitated by their fluorescence matching biological imaging window from approximately 700 to 1000 nm (CIS(Se)).[12−15] Moreover, they have already demonstrated a great potential for applications as light absorbing and emitting materials in solar cells, solar concentrators, and LEDs.[16−34] Nevertheless, the longer wavelength range of the copper chalcogenide-based nanoparticle absorption and emission is currently limited to approximately 1000 nm (CIS(Se)).[35−37] Hence, by shifting the photo-

Received: December 14, 2017
Revised: March 27, 2018
Published: March 27, 2018

DOI: 10.1021/acs.chemmater.7b05187
Chem. Mater. 2018, 30, 2607−2617

luminescence (PL) of these nanoparticles further into the near-infrared (NIR), one can significantly extend the number of their applications. Of particular importance are $CuInSe_2$ NCs, as their bulk counterpart exhibits a direct band gap of only ∼1.04 eV and relatively large exciton Bohr radius, a_B, of ∼10.6 nm.[26,38] Moreover, $CuInSe_2$ NCs possess a large absorption coefficient ($\alpha \sim 10^5$ cm^{-1}) and are able to fluoresce in the red and the NIR region in the strong quantum confinement regime ($d \ll 2a_B$, d is the NC diameter).[26,39]

Colloidal CISe NCs have been commonly prepared via several approaches such as single precursor decomposition, hydrothermal method, hot-injection, and heat-up syntheses.[3,9,10,17,28,38,40−44] By using the direct synthesis methods, the NCs are obtained in one pot, utilizing all precursors together in one reaction. Additionally, as a second step in the synthesis, a ZnS shell can be grown to enhance the PL, the stability of the NCs against oxidation, and to protect them from an aggressive environment (such as acidic media). During the past few years, the direct synthesis of CISe NCs has progressed constantly. For example, by employing bis(trimethylsilyl)-selenide as a chalcogenide precursor at relatively high temperatures (280−360 °C), Allen et al. demonstrated the synthesis of 2−6 nm CISe NCs.[35] Nose et al. synthesized 1.2−5.6 nm CISe NCs at 320 °C, whose emission shifted from 838 to 918 nm with increasing reaction time.[45] For the purpose of in vivo imaging, Cassette et al. developed a one-pot synthetic route, yielding CISe/ZnS NCs with PL spectra tunable from 700 to 1000 nm depending on the particle size (from ∼2 to ∼5 nm in diameter).[12] Zhong et al. prepared ∼3.4 nm CISe NCs at moderate temperatures (≤200 °C), which exhibited emission in the red and the NIR region (∼600−850 nm).[26]

Even though all these direct synthetic protocols enable a facile and fast reaction, some challenges concerning the complex equilibria between cation and anion precursors exhibiting different reactivities still remain. Mainly, this multicomponent reaction is limited in terms of the size, shape, and composition control of the resulting ternary and quaternary NCs. Primarily, the optical properties of small particles (≤5−6 nm) prepared by these methods, whose PL is tunable from 600 to 1000 nm, have been investigated.[9,46] Taking into account the above-mentioned limitations of the direct multicomponent colloidal synthesis, a new approach for the preparation of ternary/quaternary NCs was recently introduced by the group of Manna.[46−51] They proposed to divide the synthesis in sequential steps to achieve a more precise control over the size, shape, and composition of the NCs. Starting with the synthesis of binary chalcogenide nanoparticles, the desired trivalent cation (In^{3+}) was incorporated into the crystal lattice via a subsequent partial cation exchange (CE) reaction. This approach enables the partial replacement of host cations of a parent semiconductor NC by guest cations whereby the anion framework and thus the size and the shape of the particles are still preserved (despite the small rearrangements, especially at relatively high temperatures).[46,52] The main focus of the partial CE of copper chalcogenide-based NCs has so far been on the synthesis of C(Z)IS NCs, whereas the (sequential) partial CE to obtain CISe NCs has been rarely investigated.[14,49,50] For instance, van der Stam et al. demonstrated recently a sequential topotactic CE pathway, yielding CISe/CIS dot-in-rod core/shell nanoparticles emitting in the NIR starting from well-established CdSe/CdS nanorods preparation.[52]

In this work, we present a new synthetic approach to CISeS/ZnS NCs via a sequential partial CE starting from binary $Cu_{2-x}Se$ NCs. This new synthetic pathway enables full control over the size, shape, and composition of the resulting NCs. For the first time, homogeneous CISeS/ZnS NCs (9−18 nm in diameter) show a PL ranging from 990 to 1210 nm, depending on their size. In this method, monodisperse spherical nonstoichiometric $Cu_{2-x}Se$ NCs were prepared first via the hot-injection method. The size of the resulting NCs can be tuned by varying the reaction temperature from 170 to 220 °C, the reaction time (0.5−4 min), and the initial Cu:Se ratio. In a second step, In^{3+} ions were incorporated into the crystal lattice via partial CE. According to the initial ratio of Cu:In = 1:1, Cu^+ is partially replaced by In^{3+}. To enhance the stability of the nanoparticles and their PL properties, a ZnS shell was grown in a third step by using thiourea as a sulfur source. The as-prepared NCs exhibit a distinct dependency of their PL on the size, resulting in a wide tuning of their spectra in the NIR region.

EXPERIMENTAL SECTION

Materials. Copper(II) acetylacetonate ($Cu(acac)_2$, 97%), indium(III) acetate ($In(OAc)_3$), 99.99%), Se powder (99.99%), zinc(II) acetate ($Zn(OAc)_2$, 99.99%), dimethylformamide (DMF, 99.8%), octadecene (ODE, technical grade, 90%), octylamine (OctAm, 99%), oleylamine (OlAm, 70%), toluene (≥99.7%), and tetrachloroethylene (TCE, 99%) were purchased from Sigma-Aldrich. Tri-*n*-octylphosphine (TOP, 97%) was purchased from ABCR. Anhydrous methanol (99.9%) was purchased from VWR; thiourea (≥98%) was purchased from Merck, and 1-dodecanethiol (DDT, ≥99) was purchased from Alfa Aesar. All chemicals were used without any further purification.

Synthesis of $Cu_{2-x}Se$ Nanocrystals. The NCs were synthesized according to a method published in our recent paper.[53] First, a Se-precursor stock solution was prepared by dissolving 790 mg Se powder (10 mmol) in 5 mL of DDT and 5 mL of OlAm under vacuum at 50 °C for 1 h. The reduction by DDT led to the complete dissolution of the Se powder, resulting in a brown solution of alkylammonium selenide,[54] which was cooled to room temperature and stored in a nitrogen filled glovebox. To synthesize ∼11 nm particles (denoted as "large" throughout the text), a mixture of 262 mg of $Cu(acac)_2$ (1 mmol) in 9.5 mL of OlAm and 3 mL of DDT was degassed in a three-neck round-bottom flask under vacuum and vigorous stirring at 60 °C for 1 h. Then, the flask was filled with argon and heated to 220 °C within a short time, resulting in a yellow-orange clear solution. At this temperature, a mixture of 1 mL of the Se-precursor (1 mmol of Se) with 1.5 mL DDT (previously degassed under vacuum) was rapidly injected from a syringe into the flask upon vigorous stirring, yielding a greenish-brown solution. The temperature was maintained for 4 min with subsequent cooling to 120 °C for the further synthesis of CISe NCs (see the following section). For characterization purposes, an aliquot of the reaction mixture containing $Cu_{2-x}Se$ NCs was cooled to room temperature and was purified by the precipitation with methanol and redispersion in toluene repeated twice.

To synthesize ∼9 nm NCs, the initial Cu:Se ratio was increased to 1.25:1, thus taking 328 mg $Cu(acac)_2$ and the same amount of the Se-precursor as in the large size NC synthesis. For a further decrease of the size of the particles down to ∼8 nm, the initial Cu:Se ratio was once more increased to 1.5:1; to further reduce the size to ∼7 nm, the reaction temperature was additionally decreased to 200 °C. To further decrease the size of the particles down to ∼4 nm, the reaction temperature and the time were reduced to 170 °C and 30 s, respectively.

Synthesis of CISe NCs. As soon as the reaction mixture, as described above, was cooled down to 120 °C, a solution of 295 mg $In(OAc)_3$ (1 mmol), 9 mL ODE, 1.5 mL OlAm, 1.5 mL OctAm and 3 mL TOP (before addition of TOP, mixture was degassed at 40 °C for 30 min and subsequently filled with argon) was swiftly injected. The

DOI: 10.1021/acs.chemmater.7b05187
Chem. Mater. 2018, 30, 2607−2617

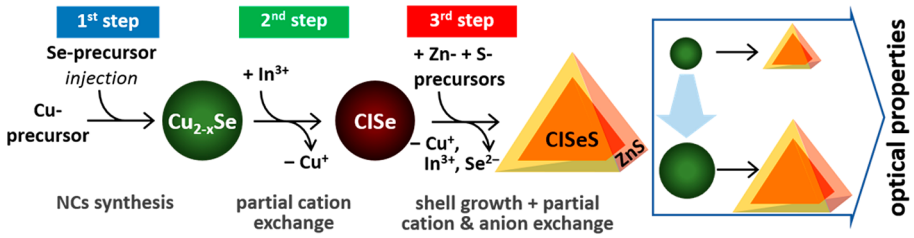

Figure 1. A scheme of the work, including the colloidal synthesis of $Cu_{2-x}Se$ NCs, their partial CE to CISe NCs, followed by the ZnS shell growth, yielding core/shell CISeS/ZnS particles. The core/shell NCs with five different sizes were used to study their optical properties.

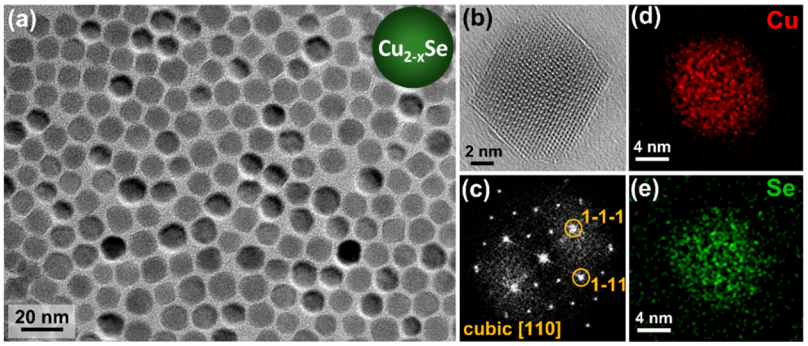

Figure 2. Conventional TEM image (a) and HRTEM image (b) of 11 nm $Cu_{2-x}Se$ NCs. Fast Fourier transform (FFT) pattern (c) and corresponding scanning TEM (STEM)-EDS maps of Cu (d) and Se (e) of an individual NC.

reaction mixture was kept at 120 °C for 20 min. An aliquot of CISe NCs was purified analogous to $Cu_{2-x}Se$ NCs for characterization purposes.

ZnS-Shell Growth. To synthesize CISeS/ZnS core/shell NCs, 1 mL of a mixture containing 1.83 g of $Zn(OAc)_2$ (10 mmol), 5 mL of OlAm, and 5 mL of OctAm (previously dissolved in a glovebox at 100 °C for 20 min) combined with 1 mL of a stock solution of 1.522 g of thiourea in 10 mL of DMF (dissolved under inert atmosphere) was injected into the crude CISe NC solution (see the previous part). The temperature of the reaction mixture was maintained at 250 °C for 20 min followed by cooling down to room temperature. For the purification of the resulting CISeS/ZnS NCs the same procedure as for the $Cu_{2-x}Se$ and CISe NCs was employed.

Transmission Electron Microscopy (TEM). For the sample preparation, a diluted NC dispersion was dropped onto a carbon coated copper grid with subsequent evaporation of the solvent. Conventional TEM imaging was carried out on a JEOL JEM-1400 microscope equipped with a thermionic gun (W filament) working at 120 kV accelerating voltage.

High Resolution Transmission Electron Microscopy (HRTEM) and Energy-Dispersive X-ray Spectroscopy (EDS). For the specimen preparation, a diluted NC dispersion was drop-cast onto ultrathin carbon/holey carbon coated 400 mesh gold grids. A JEOL JEM-2200FS microscope equipped with a 200 kV field emission gun, a CEOS spherical aberration corrector for the objective lens and an in-column image filter (Ω-type) was used for acquiring HRTEM images. EDS elemental maps and line profiles were obtained by a Bruker Quantax 400 system with a 60 mm^2 XFlash 6T silicon drift detector (SDD) mounted on this microscope. The geometric phase analysis (GPA)[55] tool for Gatan Digital Micrograph was applied to HRTEM images for direct visualization of lattice constant variation in domains with different composition within individual NCs. GPA reveals the variation in the periodicities of the lattice by analysis of the local components in the Fourier transform (FT) of the image.

Powder X-ray Diffraction (XRD). XRD patterns were recorded on a Bruker D2 Phaser using a Cu source operating at 30 kV and 10 mA. For the sample preparation, the NCs were drop-cast from concentrated dispersions onto a zero-background silicon waver. The WinXPow software with references of the Inorganic Crystal Structure Database was used for the analysis.

X-ray Photoelectron Spectroscopy (XPS). XPS was performed on an ESCALAB 250Xi X-ray Photoelectron Spectrometer Microprobe (Thermo Scientific) equipped with a monochromatized Al Kα ($h\nu$ = 1486.6 eV) X-ray source. The survey spectra were acquired at a bandpass energy of 200 eV. The high-resolution spectra (chemical state) of the detected elements were collected at the bandpass energy of 20 eV corresponding to spectral resolution of 0.5 eV. Spectra deconvolution and quantification were performed using the Avantage Data System (Thermo Scientific). For the calibration of energies of elements analyzed, we used the position of the C 1s peak corresponding to C−C bond at 284.5 eV as a reference. The samples were prepared by drop-casting a thin NC film on a precleaned Si substrate. To prevent charging, the samples were flooded with low kinetic energy electrons.

UV−Vis−NIR Absorption Spectroscopy. Absorption spectra of NCs dispersed in TCE were acquired on a Cary 5000 UV−vis−NIR spectrophotometer (Varian) using 1 cm path length quartz cuvettes.

Photoluminescence Measurements. PL spectra were measured on a FluoroLog-3 spectrofluorometer (Horiba Jobin Yvon Inc.) using excitation wavelength of 450 nm. The samples were prepared by dispersing the NCs in TCE. The PLQYs of the NIR-emitting samples were estimated using PbS quantum dots (2.8 nm diameter, absorbance peak at 875 nm, PL peak at 1000 nm)[56] emitting in the same region as a reference with PLQY 25% (determined in TCE using an integrating sphere coupled with Edinburgh Instruments FLS920 spectrofluorometer). The absolute PLQYs of the NCs emitting in the visible region were measured using a Fluorolog-3 spectrofluorometer equipped with a Quanta-φ integrating sphere.

Elemental Analysis. Inductively coupled plasma optical emission spectroscopy (ICP-OES) analysis was performed on a PerkinElmer Optima 7000DV to quantify the copper, indium, zinc, selenium, and sulfur contents in the NCs. The samples were prepared by decomposing the particles in aqua regia (HCl/HNO_3 = 3/1 (v/v)) with subsequent dilution with Milli-Q water.

Raman Spectroscopy. Raman spectra were collected by exciting samples with the 514.7 nm line of diode pumped solid state laser (Cobolt) or a 325 nm line of He−Cd laser and registered with at a spectral resolution of about 2 cm^{-1} using a LabRam HR800 micro-Raman system. For the Raman measurements, the samples were prepared by drop-casting a thin NC film on a precleaned Si substrate

DOI: 10.1021/acs.chemmater.7b05187
Chem. Mater. 2018, 30, 2607−2617

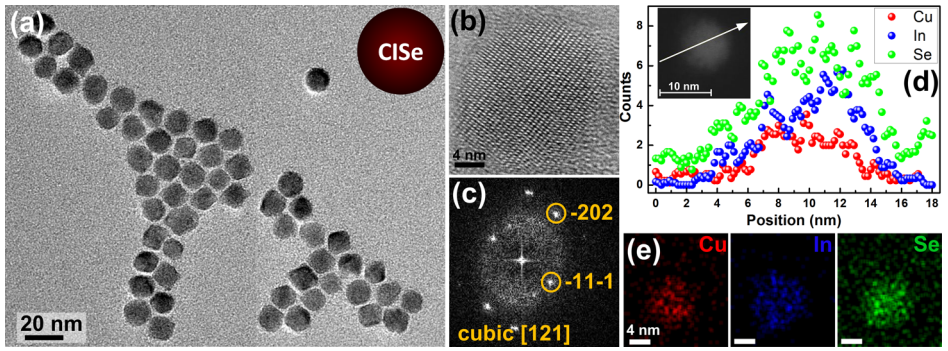

Figure 3. Conventional TEM image of partially exchanged 13.8 nm CISe NCs (a). HRTEM image (b) and corresponding FFT pattern (c) of a large CISe NC. Distribution of Cu, In, and Se acquired from a line scan over an individual nanoparticle along the arrow in the inset (d) with corresponding STEM-EDS maps (e).

(similar to the XPS analysis). The incident laser power was kept below 0.02 mW to avoid sample heating under the microscope objective (100× for 514.7 nm and 40× for 325 nm excitation).

RESULTS AND DISCUSSION

Aiming at the investigation of the size-dependent PL properties, NIR-active CISeS/ZnS NCs of different sizes were synthesized. The synthesis of CISeS/ZnS NCs was divided in three steps. First, binary $Cu_{2-x}Se$ NC samples with 5 different sizes varying from 4 to 11 nm were obtained via hot-injection. Thereafter, In^{3+} ions were incorporated into these $Cu_{2-x}Se$ NCs, forming ternary CISe nanoparticles by means of a partial CE reaction, i.e. a replacement of a part of the host copper cations by the guest indium cations in the crystal structure. Finally, a shell was grown to enhance the stability and improve the PL properties of the NCs, yielding core/shell CISeS/ZnS NC structure. A general scheme of the work is shown in Figure 1.

Synthesis of $Cu_{2-x}Se$ NCs. In the first step, non-stoichiometric $Cu_{2-x}Se$ NCs were prepared using a recently published approach.[53] Figure 2 displays the TEM images of the resulting NCs, showing fairly monodisperse spherical particles. The sizes of the particles were varied from approximately 4 to 11 nm (see Figure SI1 in the Supporting Information for the corresponding size distribution histograms) by tuning the Cu:Se ratio between the corresponding precursors in the reaction mixture, the reaction time, and the temperature. HRTEM analysis confirmed the cubic crystal structure of the NCs (Figures 2b and c), investigated in more detail in our recent paper.[53] From a quantitative analysis of a $Cu_{2-x}Se$ NC shown in the elemental maps (Figures 2d and e), the atomic ratio of Cu:Se was found to be 1.76:1, slightly larger than the previously reported value, most probably due to already investigated deviation of the elemental content from particle to particle. The thus obtained $Cu_{2-x}Se$ NCs remained in the crude solution for the following partial CE toward CISe NCs.

Synthesis of CISe NCs via Partial CE. To the crude solution of the binary nonstoichiometric $Cu_{2-x}Se$ NCs, a mixture of $In(OAc)_3$ dissolved in ODE, OlAm, OctAm, and TOP was added at the temperature of 120 °C to control the In^{3+} incorporation. The partial CE reaction was facilitated by the Cu vacancies offering to the out- and ingoing cations alternative pathways for diffusion. Furthermore, the addition of TOP plays a crucial role as it guides the direction of the CE reaction.[49] It is well-known that as a soft base TOP can easily solvate soft acid Cu^+ ions exiting the nanoparticles because of their low hardness parameter (η = 6.28),[57] thus facilitating the incorporation of In^{3+} ions into the crystal lattice followed by the $Cu^+ \rightarrow In^{3+}$ CE. Figures 3a and b present conventional and HRTEM images of the CISe particles after the CE reaction. While the quasi-spherical shape of the NCs is preserved during the CE, the average size slightly increases, ranging from 5.6 nm for small NCs to 13.6 nm for the large ones (Table 1).

Table 1. Average Size of Parent $Cu_{2-x}Se$ and Resulting CISe NCs and Cu:In Ratio in CISe NCs after Partial CE

size of $Cu_{2-x}Se$ NCs, nm	size of CISe NCs, nm	Cu:In ratio
4.3 ± 0.9	5.8 ± 0.8	1:1.66
8.3 ± 1.8	8.7 ± 1.0	1:0.99
11.3 ± 1.1	13.5 ± 1.2	1:0.97

Corresponding histograms displaying the size distribution of the NCs are presented in Figure SI2. Despite this increase in size, the anion sublattice was maintained during the CE reaction owing to the similar ionic radii of Cu^+ and In^{3+}, 77 and 72 pm, respectively.[58] FFT pattern of a single NC presented in Figure 3c reveals its cubic crystal structure, confirmed later by the XRD analysis. In this CE, the initial ratio between Cu- and In-precursors was set at 1:1, while an average Cu:In ratio in the resulting NCs was found to be 1:1−1.2 by means of ICP-OES analysis for the set of differently sized CISe particles, i.e. close to the stoichiometric composition $CuInSe_2$ (Table 1). A STEM-EDS analysis of individual particles confirmed stoichiometric composition of the samples. STEM-EDS elemental line scan and mapping revealed a homogeneous distribution of the three elements over individual NCs (Figures 3d and e).

Furthermore, we found that by increasing In concentration in the reaction mixture up to Cu:In ratio = 1:2 and 1:5, the final composition of the NCs remained close to the stoichiometric one; i.e., under the employed conditions of the synthesis, there was no further incorporation of the excess of In^{3+} ions into the structure.

Synthesis of CISeS/ZnS Core/Shell NCs. To improve the stability of the CISe NCs against oxidation and to enhance their PL, in the third step of the synthesis, the CISe NCs were covered with a ZnS shell. By adding $Zn(OAc)_2$ dissolved in OlAm and OctAm and an excess of thiourea dissolved in DMF at 250 °C, we were able to grow a thick ZnS shell around the core NCs. Figures 4a−c show the results of the TEM characterization of a series of differently sized CISeS/ZnS NCs. From the estimation of average diameters of the particles, we observed a drastic increase in their sizes after the shell growth ranging from 9 (obtained from small 4.3 nm $Cu_{2-x}Se$ NCs) to approximately 18 nm (synthesized starting from large

DOI: 10.1021/acs.chemmater.7b05187
Chem. Mater. 2018, 30, 2607−2617

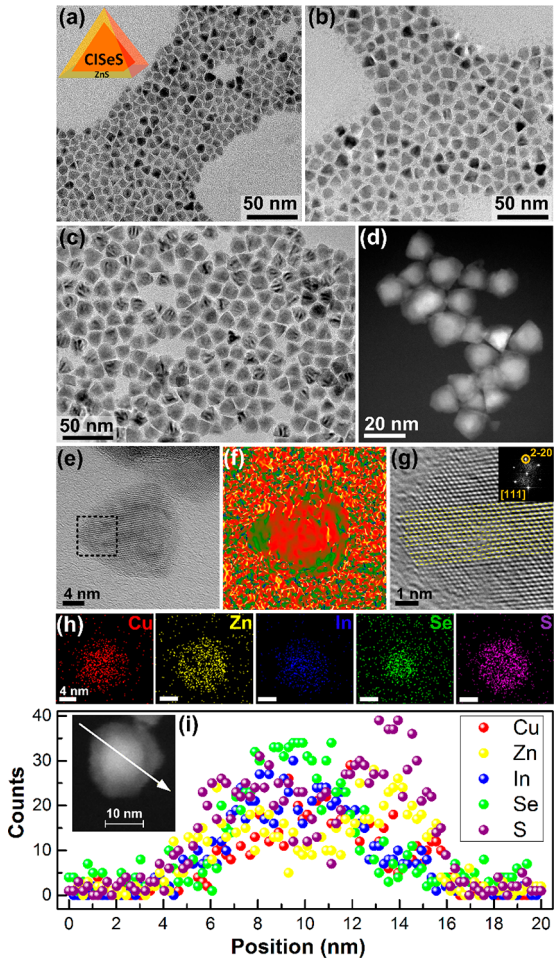

Figure 4. Conventional TEM images of small 9 nm (a), medium 11.6 nm (b), and large 17.9 nm (c) sized CISeS/ZnS NCs. HAADF-STEM image of the large NCs (d). HRTEM image of a CISeS/ZnS core/shell NC (e) with corresponding mean dilation map obtained from GPA (f), a magnified view of a region labeled by the black box in (e), and the corresponding FFT pattern (inset) (g). STEM-EDS maps of Cu, Zn, In, Se, and S (h) acquired on a large CISeS/ZnS NC with corresponding line profiles displaying the distribution of the elements across the nanoparticle (i).

10.7 nm $Cu_{2-x}Se$ NCs) CISeS/ZnS NCs (Table 2 and Figure SI3). Furthermore, the shell growth led to reshaping of the particles. Instead of quasi-spherical, the resulting CISeS/ZnS NCs exhibited a trigonal pyramidal (or tetrahedral) shape. Koo et al. already observed this type of structure during the direct colloidal synthesis of CISe NCs by the use of selenourea, CuCl, and $InCl_3$, relating the trigonal pyramidal shape to the polarity and stability of the chalcopyrite facets,[41] which can also be assumed in our CISeS/ZnS NC structure.

Table 2. Average Size and Composition of the Series of CISeS/ZnS Core/Shell NCs

size, nm	ratio Cu:In:Se:Zn:S
9.0 ± 1.2	1:1.17:0.38:1.05:2.54
10.6 ± 2.2	1:1.04:0.52:0.87:2.3
11.6 ± 1.7	1:1.11:0.59:0.89:2.14
13.9 ± 2.2	1:1.11:0.81:0.45:1.58
17.9 ± 1.7	1:1.13:0.67:1.25:2.46

The average composition of the CISeS/ZnS core/shell NCs determined by means of ICP-OES is presented in Table 2. The results of the analysis demonstrate a decrease of the average Cu:In ratio in the NCs after the shell growth as compared to the CISe NC cores, suggesting additional incorporation of indium cations as well as a replacement of copper ions by zinc in the core ($Cu^+ \rightarrow Zn^{2+}$). We do not exclude simultaneous $In^{3+} \rightarrow Zn^{2+}$ CE reaction, although it should be less efficient than the $Cu^+ \rightarrow Zn^{2+}$ one. An average Cu:In ratio (1.14) can be considered constant among the three NC sizes. Much more striking is the dramatic decrease of the Se content in the NCs after the shell growth, falling below its stoichiometric value for all three sizes, among which the lowest content was found in the small NCs with Cu:Se ratio = 0.38. With increasing the NC size, the Se content rises, reaching Cu:Se ratio of 0.67 in the large NC sample. This lack of the host anion is compensated by sulfur, which is present in the particles in large excess compared to the content of zinc, with which in the case of a pure ZnS shell formation it should be in an equivalent proportion. These two clear trends imply that, in addition to the Cu^+ (In^{3+}) → Zn^{2+} CE, we observe more pronounced anion exchange process in which sulfur, present in large amounts in the form of thiourea used as the S-precursor, and DDT employed as one of the ligands, replaces selenium in the core CISe NCs, yielding in fact quasi-quinary Cu−Zn−In−Se−S alloy structure, as supported by Raman data presented in the next section. In this scenario, with the increasing size of the core particles, the efficiency of the anion exchange drops, indicated by the above-mentioned increase of the Se content. This distinct anion exchange is possible owing to an efficient extraction of Se by TOP ligand from the CISe NCs, a process similar to what we recently observed on the example of $Cu_{2-x}Se$ NCs.[53] In that case, highly copper deficient $Cu_{2-x}Se$ NCs lost almost 20% of selenium in the presence of TOP already at room temperature. This removal might be facilitated at a higher temperature (250 °C) used to grow the ZnS shell.

To gain a further insight into the structure of the particles, high angular annular dark field (HAADF)-STEM imaging and STEM-EDS mapping were carried out on the large sized CISeS/ZnS NCs (Figures 4d, h, and i). HAADF-STEM characterization reveals the formation of a thick ZnS shell evident by a clear contrast difference between the core, which appears lighter, and the shell, which appears darker in the image. Elemental ratio of Cu:In:Se:Zn:S = 1:0.9:1:1.1:1.8 obtained on an individual NC confirms the large excess of sulfur present in the particles. The mean dilation map in Figure 4f was obtained by applying GPA to the HRTEM image of a CISeS/ZnS NC presented in Figure 4e (a central area of the NC was selected as a reference). The results show that the dilatation is −6.9 ± 1.9% in the green area relative to the central area. Considering a_{ZnS} = 5.32 Å (ICSD card 41985), the central area has a lattice constant of 5.71 ± 0.11 Å. The magnified view of the region in the black box in Figure 4e and its corresponding FFT pattern demonstrate the epitaxial relationship between the core and the shell: CISe [111] // ZnS [111], CISe (2−20) // ZnS (2−20) (Figure 4g).

Elemental line profiles in Figure 4i imply the presence of sulfur in the core with its highest content located on the core surface. Copper and indium are uniformly distributed over the core region of the particles, whereas selenium is mostly accumulated in the very center of the NC. One can expect anion exchange being more efficient on the surface of a NC because the size of anions (in particular chalcogen ions) is

DOI: 10.1021/acs.chemmater.7b05187
Chem. Mater. 2018, 30, 2607−2617

much larger than that of cations, which should hinder the exchange reaction, limiting it by the surface region. Thus, combining the results of ICP-OES and STEM-EDS analyses, we conclude that overall the core/shell NCs are built of CISe-rich cores with significant inclusion of S accumulated mostly on the surface of the particles, which is confirmed also by the increasing amount of Se with increasing the NC size and by the formation of a ZnS-rich shell.

When the ZnS shell growth was performed in the presence of an excess of the In precursor mentioned in the previous section (Cu:In feed ratio = 1:2 and 1:5), we observed a drastic increase of the indium content in the resulting particles (see Table SI1). In both cases, the final ratio of the copper and indium ions in the NCs was close to the initial one, i.e. 1:2.06 (from initial 1:2) and 1:5.9 (from initial 1:5). These experiments demonstrate that at a higher temperature $Cu^{+} \rightarrow In^{3+}$ CE is more efficient, and it is possible to incorporate large amounts of indium significantly exceeding its stoichiometric content.

Raman Characterization. The structure and composition of the NCs derived above was further affirmed by Raman spectroscopy. Raman spectra of a series of the large particles, including $Cu_{2-x}S$, CISe, and CISeS/ZnS NCs, are shown in Figure 5. For $Cu_{2-x}Se$ NCs, the main Raman mode at 262.5

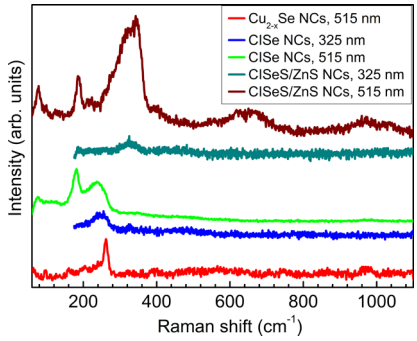

Figure 5. Raman spectra of large $Cu_{2-x}Se$, CISe, and CISeS/ZnS NCs, measured at 515 and 325 nm excitation (see text for details).

cm^{-1} is in agreement with previous reports on bulk CuSe (263 cm^{-1})[59] and $Cu_{2-x}Se$ NCs (260 cm^{-1}).[53] This mode is absent in the spectrum of CISe NCs, indicating efficient transformation of $Cu_{2-x}Se$ NCs into CISe. No $Cu_{2-x}S$ phase was detected. Position of the CISe mode in the initial CISe NCs, 181 cm^{-1}, is slightly higher than 177 cm^{-1} for CISe of chalcopyrite structure,[60] the solely CISe modification studied by Raman up to now. The higher frequency in our case is most likely related to different phase (cubic) because perceptible shifts induced by phonon confinement are observed in Raman spectra only for NCs smaller than 10 nm.[61] The observed phonon frequency can therefore be characteristic of the cubic CISe phase. For the CIS counterpart, for instance, the wurtzite was supposed to possess higher frequency of the main phonon as compared to the chalcopyrite one.[62] The upward shift of the main CISe mode in the core/shell NCs by 7 cm^{-1} can be related with S-interdiffusion, with the corresponding x value of $CuIn(S_xSe_{1-x})_2$ alloy around 0.2.[60] The broad amorphous-like feature in the CISe NC spectrum peaked around 240 cm^{-1} can be related with residual $Cu_{2-x}Se$ or Se phases, presumably on the NC surface, which was not converted into CISe. Suppression of this broad feature in the spectrum of core/shell NCs supports its surface relation. This assumption is in agreement with XPS results which show some elemental Se contribution in CISe but not in CISeS/ZnS NCs (see the next section). The broad spectral feature that dominates the spectrum of the core/shell NCs at visible excitation (i.e., resonant with the CISe NC core) can be related to Zn−S bond vibration in the alloy with CISe. We observed similar Raman features for several related alloyed NC systems recently.[63−65] No noticeable volume of pure ZnS phase is supposed to be formed, as follows from the absence of the vibration characteristic for pure ZnS lattice (~350 cm^{-1}) at the 325 nm excitation. The latter wavelength is resonant with ZnS bandgap, and one readily observes even thin ZnS shell at this excitation, as we recently reported for CIS/ZnS system.[65]

Therefore, the Raman data confirm that in the core/shell NCs, we have CISe- and ZnS-rich regions, apparently the core and the shell, respectively. The broad features at 650 and 970 cm^{-1} can be assigned to the second and third order of the Zn−S vibration band at 330 cm^{-1}, indicating the high crystallinity of the alloyed lattice.[65]

XRD Characterization. Further, we studied the crystal structure of the NCs from three steps of the synthesis via XRD analysis (Figure 6). Its results confirmed a cubic berzelianite

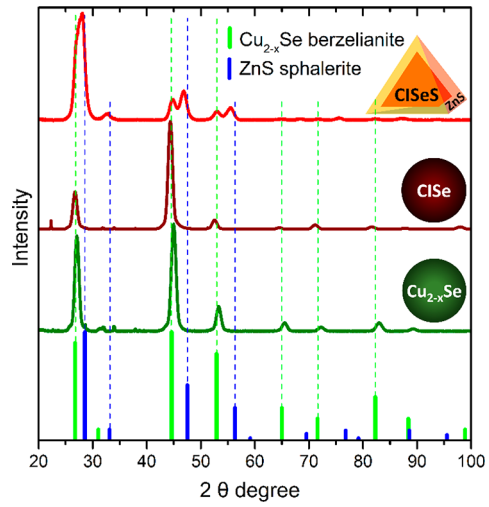

Figure 6. XRD patterns of $Cu_{2-x}Se$, CISe NCs after partial CE, and CISeS/ZnS core/shell NCs after the shell growth. The experimental XRD patterns are compared to database powder diffraction files of cubic berzelianite (ICSD C6-680) and cubic zinc sulfide sphalerite (ICSD C5-566).

phase of the parent $Cu_{2-x}Se$ NCs, investigated in our previous work.[53] The reflexes are slightly shifted to larger Bragg angles due to a large number of the copper vacancies in the crystal lattice.[53] After the In incorporation by means of partial CE, this cubic crystal structure was maintained, being accompanied by a slight change of the ratio between intensities of the main reflexes. The reflexes of this crystal phase are shifted to smaller angles because of the simultaneous filling of the copper vacancies during the partial CE reaction, a process similar to what we observed comparing copper deficient and stoichiometric copper selenide NCs.[53] The XRD pattern of the NCs after the shell growth indicates two main crystal phases corresponding to the preserved cubic berzelianite structure of the CISe-rich core and newly formed cubic zinc sphalerite phase of the shell. The domination of the reflexes of the latter confirms the formation of large ZnS-rich crystallites, i.e. a thick shell. The maintenance of the cubic crystal structure of the core

DOI: 10.1021/acs.chemmater.7b05187
Chem. Mater. 2018, 30, 2607−2617

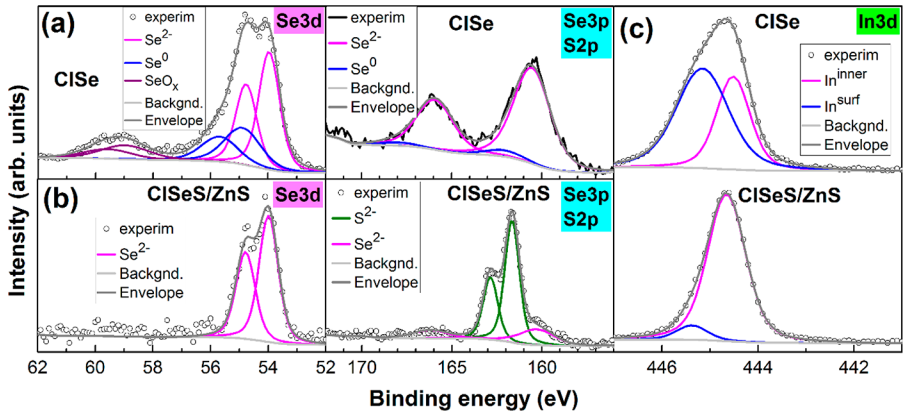

Figure 7. High-resolution XPS scans on Se 3d and S 2p–Se 3p (a, b) and In 3d (c) peaks of large CISe and CISeS/ZnS NCs, along with the peak fitting.

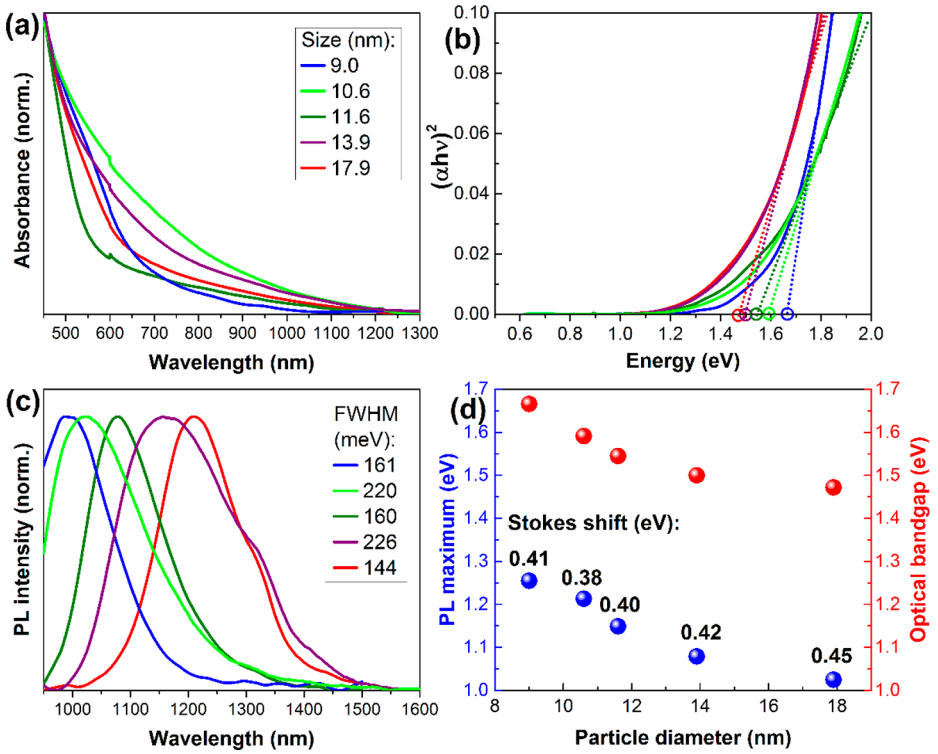

Figure 8. Absorption spectra of CISeS/ZnS core/shell NCs with five different sizes (a) and corresponding Tauc plots (b). PL spectra of differently sized CISeS/ZnS NCs (c) with corresponding relation between PL maxima (blue), optical bandgap (red), and the size of the NCs (d). Values of full width at half maxima of the PL spectra are indicated in panel (c); Stokes shift values are shown in panel (d).

despite of the partial anion exchange shows its thermodynamic stability and thus allows it to template the growth of a similar cubic ZnS lattice. Taking into account the reshaping of the particles, we may assume a slight rearrangement of the cubic lattice to the tetragonal one (chalcopyrite), having very similar main reflexes,[41] that does not allow for an unambiguous discrimination between these two phases. The shift of the ZnS-related reflexes to smaller angles occurs due to contribution from Se incorporated into the shell at the interface, yielding alloyed ZnS_xSe_{1-x} thick shell, revealed by the Raman spectroscopy. The thickness of the shell determined by using the Debye–Scherrer formula was found to be 5.7 nm for the large 17.9 nm particles.

XPS Characterization. To further study the structure of the synthesized NCs, we characterized them by means of the XPS analysis, which is known to probe mainly the surface of the nanoparticles. As follows from the results presented in Figures 7 and SI4, in $Cu_{2-x}Se$ NCs, the ratio Cu:Se = 1.4:1 is in agreement with the expected Cu-deficient structure and suggests a lower Cu content on the surface of the NCs in comparison with the results of the STEM-EDS measurements. After the partial $Cu^+ \rightarrow In^{3+}$ CE XPS reveals the ratio Cu:In = 1:1.6 in CISe nanoparticles, which implies only a small deviation from the ICP-OES and the STEM-EDS data. Comparing the composition of the CISe NCs determined by ICP-OES and STEM-EDS with that measured by XPS, we may conclude that the surface of the particles is In- and Se-rich, which means that CE in the large particles occurs mainly close to the surface, leaving Cu-rich core. Following the data analysis, in the CISeS/ZnS NCs, the ratio Cu:In:Se:Zn:S =

DOI: 10.1021/acs.chemmater.7b05187
Chem. Mater. 2018, 30, 2607–2617

1:1.2:0.8:1:2.2 is in agreement with the ratio determined by ICP-OES and STEM-EDS showing only small deviations toward higher content of In, Zn, and S, which corroborates the fact that predominantly the outer part of the NC contributes to the XPS signal. A further comparison with the XPS results of the CISe NCs reveals Cu signal having the same sharp single peak with the same binding energies for both samples (the core and the core/shell particles) (Figure SI4a), indicating that Cu is not exposed at the surface and as a result is also not affected by the deposition of the shell, which agrees with the STEM-EDS results. Furthermore, the comparison displays the decrease of In and Se contents with respect to Cu in the core/shell NCs, yielding the Cu:In ratio close to 1:1 (Figure SI4b, c). A strong decrease of the detected Se content in the core/shell structure can further be related to the interdiffusion of S (100% excess compared to Zn) and thus partial substitution of Se in other parts of the core, which was already confirmed by analyzing the ICP-OES and STEM-EDS data. The S^{2-} XPS signal is observed as a sharp 2p doublet centered at approximately 163 eV on top of the Se 3p spectra (Figure 7b). The structure of the NCs resembles an intermixed/alloyed structure with a S- and Zn-rich shell in which both S and Se contribute to the lattice, which is in good agreement with the previous observations. Furthermore, the XPS results show that deposition of the ZnS shell removes the minor contribution of the elemental Se (Se^0) and oxidized Se (SeO_x), most likely residing on the surface of the CISe NCs, leaving only a sharp single Se^{2-} component (cf. Figures 7a and b). Similarly, suppression of the surface component of In in CISeS/ZnS is observed in XPS spectra, yielding a domination of the component corresponding to fully coordinated atoms of the interior of the NCs (Figure 7c) and confirms the formation of a continuous shell.

Optical Properties of $Cu_{2-x}Se$, CISe, and CISeS/ZnS NCs. The samples obtained were further characterized by means of absorption and PL spectroscopy to relate their size and structure with the optical properties. Absorption spectra of large $Cu_{2-x}Se$, CISe, and CISeS/ZnS NCs are displayed in Figure SI5. Parent $Cu_{2-x}Se$ NCs possessed a strong localized surface plasmon resonance in the NIR region attributed to the collective oscillation of holes[66] with an absorption maximum at approximately 1150 nm, which was damped after the $Cu^+ \rightarrow In^{3+}$ CE, indicating a complete filling of Cu vacancies.[53,67,68] The absorption spectrum of the resulting CISe NCs does not exhibit well-defined features, which is a typical behavior for large CIS and CISe NCs. One possible reason for this featureless absorption is an inhomogeneous composition of the particles within the ensemble.[69,70] As can be seen in Figure SI5, the shape of the spectrum remains essentially the same after the shell growth, although its onset shifts to shorter wavelengths, from approximately 1400 to 1300 nm, implying the increase of the optical band gap due to the incorporation of zinc and sulfur ions into the CISe core. This trend is opposite to that commonly observed in II−VI quantum dots, where the shell growth leads to a prominent red shift due to a reduced quantum confinement (usually caused by the delocalization of the electron wave function over the shell).[71]

The dependency of the absorption band on the size of the core/shell NCs is shown in Figure 8a. Compared to the large- and medium-sized particles, whose absorption onsets are at approximately 1300 nm, the small NCs start to absorb at approximately 1060 nm, i.e. their optical band gap is wider, as expected from the size relation due to quantum confinement. A more detailed information of the relation between the optical properties and the size of the NCs is demonstrated in Figure 8b. Based on the absorption spectra, the direct optical band gaps ($E_{g,opt}$) of the differently sized CISeS/ZnS NCs can be determined by extrapolation of the linear region of the Tauc plots ($(\alpha h\nu)^2$ versus energy, where α is the corresponding absorption and $h\nu$ is the photon energy). This plotting resulted in $E_{g,opt}$ values shown in Figure 8d. The values increase by decreasing the particle size, as one may expect, which confirms a relation between the size and the optical properties of these NCs. Here, we note that in addition to the size of the NCs, the band gap values can be affected by the variation of the composition of the particles resulted from the incorporation of both zinc and sulfur into the CISe core. We also have to admit that in the case of samples with unstructured absorption spectra, Tauc plotting should be used with care, as it does not provide unambiguously precise values of optical gaps. For their determination, we used quite broad energy range of absorption (Figure 8b). Nevertheless, the results demonstrate a clear trend in the variation of the $E_{g,opt}$ values with the size, where the energy decrease is nonlinear but rather tends to a plateau with increasing the size.

A further analysis of the optical properties of the NCs was performed by using PL data presented in Figure 8c. The broad PL bands and the large Stokes shifts are characteristic for this type of NC and commonly explained by a complex dynamics of the radiative carrier recombination through a midgap acceptor state. Thus, Debnath et al. assumed that antisite defect states are created during the growth of CIS NCs when Cu^+ occupies the site in a crystal which is normally occupied by an In^{3+} ion.[72] As a consequence, the antisite defects introduce midgap states with energy levels higher than the valence band edge.[50,72,73] In some cases, even more complex model is used to explain optical properties of these nanoparticles, according to which the recombination of an exciton occurs through both acceptor and donor states. In this scenario, electron and hole created after excitation first nonradiatively relax to these midgap states and then radiatively recombine. For relatively large CIS/ZnS quantum dots, we recently confirmed the first recombination pathway, i.e. through the acceptor state above the valence band edge of the material.[46] In the studied set of samples, we observe a strong dependence of the PL spectra positions on the size of the NCs (Figures 8c and d), where the small particles exhibited a PL maximum at 990 nm, while the PL maxima for the medium and the large sized NCs were located at 1020, 1080, 1160, and 1210 nm, respectively. Thus, by increasing the particle size, the PL maximum was shifted to longer wavelengths farther into the NIR spectral region. This relation between the size and the optical properties of the NCs is summarized in Figure 8d, where both graphs show a strong correlation between the PL maximum/optical bandgap and the size of the NCs. Therefore, our results demonstrate the possibility of the tuning of optical properties of CISe-based NCs on the wide range in the NIR region with the emission of the largest sample centered at 1210 nm which, to the best of our knowledge, is the farthest achieved PL for this material so far, and which actually goes beyond the bulk band gap of CISe (~1190 nm)[26] owing to a complex mechanism of the exciton recombination leading to a large Stokes shift of 0.4−0.45 eV. The Stokes shift values coincide reasonably well with data reported for similar NCs possessing a more structured absorption; for example, 0.53 eV was determined for CISeS/ZnS NCs,[20] 0.4 eV for CISeS NCs,[36] 0.25−0.4 eV for CIS NCs of different sizes,[74] and 0.46 eV for CIS NCs.[75] This match also

DOI: 10.1021/acs.chemmater.7b05187
Chem. Mater. 2018, 30, 2607−2617

validates our determination of the $E_{g,opt}$ values via Tauc plots. It is important to note that the PL broadening of our samples (full width at half-maximum (fwhm) value) is narrower than typically reported values for analogous NCs, >300 meV[76] (Figure 8c). Even samples with relatively broad size distributions (with average sizes 10.3 and 14.1 nm) exhibit fwhm values of about 220 meV, whereas the other NC samples display narrower PL bands. This nicely proves that the CE strategy offers a more precise control over the sizes and compositions of copper chalcogenide-based NCs than their direct synthesis.

It is interesting to note that incorporation of a large amount of indium into the NCs described above led to a strong blue-shift of the PL to the visible region. We observed PL maxima of the two samples with Cu:In ratios of 1:2.06 and 1:5.9 at approximately 615 and 660 nm, respectively, with broad spectral profiles (Figure SI6). In the absorption spectra, a defined shoulder appeared at approximately 510 nm.

PLQYs of the CISeS/ZnS NC samples were estimated by comparing their emission spectra (normalized to absorption at the excitation wavelength, 450 nm) with that of PbS quantum dots used as a reference with well-characterized PLQY = 25%. All samples exhibited rather low PLQY values below 1%, which can be explained by a weak quantum confinement regime, as the size of these NCs approach the double Bohr radius of CISe (21.2 nm).[26,38] In addition, as demonstrated by the structural analyses, the actual composition of our core NCs is rather CISeS alloy. Therefore, one may expect a decrease of the Bohr radius in this compound falling between that of the pure CISe and the pure CIS (4.1 nm).[11] Another possible reason of the weak PL might be a small amount of centers for radiative recombination in these NCs, namely Cu^{2+} defects.[74,76,77] These defects have been elucidated as main recombination centers in CIS NCs in a recent work of the Brovelli's and Klimov's groups, which can be valid also for CISe-based materials. It is interesting to note that In-rich samples emitting in the visible region exhibited higher QY values of 5%. We therefore will focus our further investigations on the control over the Cu^{2+} defects in the crystal structure of CISeS/ZnS NCs.

CONCLUSIONS

We developed an approach to NIR-active copper indium selenide-based NCs via sequential partial cation exchang reactions. Starting with the synthesis of copper deficient binary $Cu_{2-x}Se$ NCs of different sizes, a subsequent cation exchange with In^{3+} led to the formation of ternary CISe NCs. While the shape of these NCs was preserved, their size increased as a consequence of the incorporation of In^{3+} ions. The Cu:In ratio was controlled to be 1:1 by the use of moderate temperatures and a feed precursor ratio of 1:1. By covering the NCs with ZnS shells, CISeS/ZnS NCs were synthesized, forming alloyed structures with ZnS-rich shell. In this process, for the first time, we observed a prominent anion exchange $Se^{2-} \rightarrow S^{2-}$, whose efficiency was dependent on the size of the core nanoparticles being limited by the surface region. The shell growth resulted in a drastic increase in the size and reshaping the particles from spheres to trigonal pyramids while preserving their crystal structure. Furthermore, we were able to cover a wide range of the photoluminescence with maxima from 990 to 1210 nm by varying the particle size while keeping the spectra relatively narrow for this type of semiconductor nanoparticles. Thus, we were able to push the PL maxima to longer wavelengths with the large CISeS/ZnS NCs exhibiting the farthest for this material emission in the NIR, which goes beyond the bulk band gap of CISe. We believe that our results provide not only new insights into the mechanism of cation/anion exchange reactions but also constitute a general strategy to synthesize a wide variety of copper chalcogenide-based nanocrystals with precisely controlled sizes and compositions.

ASSOCIATED CONTENT

Supporting Information

The Supporting Information is available free of charge on the ACS Publications website at DOI: 10.1021/acs.chemmater.7b05187.

Size distribution histograms of $Cu_{2-x}Se$, CISe, and CISeS/ZnS NCs; additional XPS scans; absorption spectra of large sized $Cu_{2-x}Se$, CISe, and CISeS/ZnS NCs; ICP-OES results; absorption and PL spectra of CISeS/ZnS core/shell NC samples with large indium content (PDF)

AUTHOR INFORMATION

Corresponding Author

*E-mail: vladimir.lesnyak@chemie.tu-dresden.de.

ORCID

Iwan Moreels: 0000-0003-3998-7618

Vladimir Lesnyak: 0000-0002-2480-8755

Author Contributions

⊥J.F.L.L. and Z.D. equally contributed to this work.

Notes

The authors declare no competing financial interest.

ACKNOWLEDGMENTS

We are grateful to S. Goldberg (TU Dresden) for TEM imaging, F. Eichler for quantum yield measurements, and to R. Schulze and for ICP-OES measurements. V.D. and D.R.T.Z. acknowledge the Volkswagen Foundation (Project 90366) for support. Z.D. acknowledges the funding from the European Union under Grant Agreement 614897 (ERC Grant TRANS-NANO). B.M.-G. acknowledges the funding received from the EU Horizon 2020 research and innovation program under Grant Agreement 696656 (GrapheneCore1). This work was supported by the German Research Foundation (DFG) under the project LE 3877/1-1 and by the EU Horizon 2020 project MiLEDi (779373).

REFERENCES

(1) Scholes, G. D. Controlling the Optical Properties of Inorganic Nanoparticles. *Adv. Funct. Mater.* **2008**, *18*, 1157−1172.

(2) Talapin, D. V.; Lee, J.-S.; Kovalenko, M. V.; Shevchenko, E. V. Prospects of Colloidal Nanocrystals for Electronic and Optoelectronic Applications. *Chem. Rev.* **2010**, *110*, 389−458.

(3) Kovalenko, M. V.; Manna, L.; Cabot, A.; Hens, Z.; Talapin, D. V.; Kagan, C. R.; Klimov, V. I.; Rogach, A. L.; Reiss, P.; Milliron, D. J.; Guyot-Sionnnest, P.; Konstantatos, G.; Parak, W. J.; Hyeon, T.; Korgel, B. A.; Murray, C. B.; Heiss, W. Prospects of Nanoscience with Nanocrystals. *ACS Nano* **2015**, *9*, 1012−1057.

(4) Sapsford, K. E.; Algar, W. R.; Berti, L.; Gemmill, K. B.; Casey, B. J.; Oh, E.; Stewart, M. H.; Medintz, I. L. Functionalizing Nanoparticles with Biological Molecules: Developing Chemistries that Facilitate Nanotechnology. *Chem. Rev.* **2013**, *113*, 1904−2074.

(5) Kagan, C. R.; Lifshitz, E.; Sargent, E. H.; Talapin, D. V. Building Devices from Colloidal Quantum Dots. *Science* **2016**, *353*, 885.

DOI: 10.1021/acs.chemmater.7b05187
Chem. Mater. 2018, 30, 2607−2617

(6) Carey, G. H.; Abdelhady, A. L.; Ning, Z.; Thon, S. M.; Bakr, O. M.; Sargent, E. H. Colloidal Quantum Dot Solar Cells. *Chem. Rev.* **2015**, *115*, 12732−12763.
(7) Kramer, I. J.; Sargent, E. H. The Architecture of Colloidal Quantum Dot Solar Cells: Materials to Devices. *Chem. Rev.* **2014**, *114*, 863−882.
(8) Tamang, S.; Lincheneau, C.; Hermans, Y.; Jeong, S.; Reiss, P. Chemistry of InP Nanocrystal Syntheses. *Chem. Mater.* **2016**, *28*, 2491−2506.
(9) Aldakov, D.; Lefrancois, A.; Reiss, P. Ternary and Quaternary Metal Chalcogenide Nanocrystals: Synthesis, Properties and Applications. *J. Mater. Chem. C* **2013**, *1*, 3756−3776.
(10) Coughlan, C.; Ibáñez, M.; Dobrozhan, O.; Singh, A.; Cabot, A.; Ryan, K. M. Compound Copper Chalcogenide Nanocrystals. *Chem. Rev.* **2017**, *117*, 5865−6109.
(11) Kolny-Olesiak, J.; Weller, H. Synthesis and Application of Colloidal $CuInS_2$ Semiconductor Nanocrystals. *ACS Appl. Mater. Interfaces* **2013**, *5*, 12221−12237.
(12) Cassette, E.; Pons, T.; Bouet, C.; Helle, M.; Bezdetnaya, L.; Marchal, F.; Dubertret, B. Synthesis and Characterization of Near-Infrared Cu-In-Se/ZnS Core/Shell Quantum Dots for In Vivo Imaging. *Chem. Mater.* **2010**, *22*, 6117−6124.
(13) Li, L.; Daou, T. J.; Texier, I.; Chi, T. T. K.; Liem, N. Q.; Reiss, P. Highly Luminescent $CuInS_2$/ZnS Core/Shell Nanocrystals Cadmium-Free Quantum Dots for In Vivo Imaging. *Chem. Mater.* **2009**, *21*, 2422−2429.
(14) Guo, W.; Chen, N.; Tu, Y.; Dong, C.; Zhang, B.; Hu, C.; Chang, J. Synthesis of Zn-Cu-In-S/ZnS Core/Shell Quantum Dots with Inhibited Blue-Shift Photoluminescence and Applications for Tumor Targeted Bioimaging. *Theranostics* **2013**, *3*, 99−108.
(15) Pons, T.; Pic, E.; Lequeux, N.; Cassette, E.; Bezdetnaya, L.; Guillemin, F.; Marchal, F.; Dubertret, B. Cadmium-Free $CuInS_2$/ZnS Quantum Dots for Sentinel Lymph Node Imaging with Reduced Toxicity. *ACS Nano* **2010**, *4*, 2531−2538.
(16) Song, W.-S.; Yang, H. Efficient White-Light-Emitting Diodes Fabricated from Highly Fluorescent Copper Indium Sulfide Core/Shell Quantum Dots. *Chem. Mater.* **2012**, *24*, 1961−1967.
(17) Panthani, M. G.; Stolle, C. J.; Reid, D. K.; Rhee, D. J.; Harvey, T. B.; Akhavan, V. A.; Yu, Y.; Korgel, B. A. $CuInSe_2$ Quantum Dot Solar Cells with High Open-Circuit Voltage. *J. Phys. Chem. Lett.* **2013**, *4*, 2030−2034.
(18) McDaniel, H.; Fuke, N.; Makarov, N. S.; Pietryga, J. M.; Klimov, V. I. An Integrated Approach to Realizing High-Performance Liquid-Junction Quantum Dot Sensitized Solar Cells. *Nat. Commun.* **2013**, *4*, 2887.
(19) Panthani, M. G.; Akhavan, V.; Goodfellow, B.; Schmidtke, J. P.; Dunn, L.; Dodabalapur, A.; Barbara, P. F.; Korgel, B. A. Synthesis of $CuInS_2$, $CuInSe_2$, and $Cu(In_xGa_{1-x})Se_2$ (CIGS) Nanocrystal "Inks" for Printable Photovoltaics. *J. Am. Chem. Soc.* **2008**, *130*, 16770−16777.
(20) Meinardi, F.; McDaniel, H.; Carulli, F.; Colombo, A.; Velizhanin, K. A.; Makarov, N. S.; Simonutti, R.; Klimov, V. I.; Brovelli, S. Highly Efficient Large-Area Colourless Luminescent Solar Concentrators Using Heavy-Metal-Free Colloidal Quantum Dots. *Nat. Nanotechnol.* **2015**, *10*, 878−885.
(21) Stolle, C. J.; Harvey, T. B.; Pernik, D. R.; Hibbert, J. I.; Du, J.; Rhee, D. J.; Akhavan, V. A.; Schaller, R. D.; Korgel, B. A. Multiexciton Solar Cells of $CuInSe_2$ Nanocrystals. *J. Phys. Chem. Lett.* **2014**, *5*, 304−309.
(22) Akhavan, V. A.; Goodfellow, B. W.; Panthani, M. G.; Steinhagen, C.; Harvey, T. B.; Stolle, C. J.; Korgel, B. A. Colloidal CIGS and CZTS Nanocrystals: A Precursor Route to Printed Photovoltaics. *J. Solid State Chem.* **2012**, *189*, 2−12.
(23) Lesyuk, R.; Cai, B.; Reuter, U.; Gaponik, N.; Popovych, D.; Lesnyak, V. Quantum-Dot-in-Polymer Composites via Advanced Surface Engineering. *Small Methods* **2017**, *1*, 1700189.
(24) Kim, S.; Kang, M.; Kim, S.; Heo, J.-H.; Noh, J. H.; Im, S. H.; Seok, S. I.; Kim, S.-W. Fabrication of $CuInTe_2$ and $CuInTe_{2-x}Se_x$ Ternary Gradient Quantum Dots and Their Application to Solar Cells. *ACS Nano* **2013**, *7*, 4756−4763.
(25) Guo, Q.; Ford, G. M.; Hillhouse, H. W.; Agrawal, R. Sulfide Nanocrystal Inks for Dense $Cu(In_{1-x}Ga_x)(S_{1-y}Se_y)_2$ Absorber Films and Their Photovoltaic Performance. *Nano Lett.* **2009**, *9*, 3060−3065.
(26) Zhong, H.; Wang, Z.; Bovero, E.; Lu, Z.; van Veggel, F. C. J. M.; Scholes, G. D. Colloidal $CuInSe_2$ Nanocrystals in the Quantum Confinement Regime: Synthesis, Optical Properties, and Electroluminescence. *J. Phys. Chem. C* **2011**, *115*, 12396−12402.
(27) Cao, S.; Ji, W.; Zhao, J.; Yang, W.; Li, C.; Zheng, J. Color-Tunable Photoluminescence of Cu-Doped Zn-In-Se Quantum Dots and Their Electroluminescence Properties. *J. Mater. Chem. C* **2016**, *4*, 581−588.
(28) Guo, Q.; Kim, S. J.; Kar, M.; Shafarman, W. N.; Birkmire, R. W.; Stach, E. A.; Agrawal, R.; Hillhouse, H. W. Development of $CuInSe_2$ Nanocrystal and Nanoring Inks for Low-Cost Solar Cells. *Nano Lett.* **2008**, *8*, 2982−2987.
(29) Chen, B.; Zhong, H.; Zhang, W.; Tan, Z. a.; Li, Y.; Yu, C.; Zhai, T.; Bando, Y.; Yang, S.; Zou, B. Highly Emissive and Color-Tunable $CuInS_2$-Based Colloidal Semiconductor Nanocrystals: Off-Stoichiometry Effects and Improved Electroluminescence Performance. *Adv. Funct. Mater.* **2012**, *22*, 2081−2088.
(30) Zhang, W.; Lou, Q.; Ji, W.; Zhao, J.; Zhong, X. Color-Tunable Highly Bright Photoluminescence of Cadmium-Free Cu-Doped Zn-In-S Nanocrystals and Electroluminescence. *Chem. Mater.* **2014**, *26*, 1204−1212.
(31) Weil, B. D.; Connor, S. T.; Cui, Y. $CuInS_2$ Solar Cells by Air-Stable Ink Rolling. *J. Am. Chem. Soc.* **2010**, *132*, 6642−6643.
(32) Sumner, R.; Eiselt, S.; Kilburn, T. B.; Erickson, C.; Carlson, B.; Gamelin, D. R.; McDowall, S.; Patrick, D. L. Analysis of Optical Losses in High-Efficiency $CuInS_2$-Based Nanocrystal Luminescent Solar Concentrators: Balancing Absorption versus Scattering. *J. Phys. Chem. C* **2017**, *121*, 3252−3260.
(33) Zaiats, G.; Ikeda, S.; Kinge, S.; Kamat, P. V. Quantum Dot Light-Emitting Devices: Beyond Alignment of Energy Levels. *ACS Appl. Mater. Interfaces* **2017**, *9*, 30741−30745.
(34) Lesyuk, R.; Lesnyak, V.; Herguth, A.; Popovych, D.; Bobitski, Y.; Klinke, C.; Gaponik, N. Simulation Study of Environmentally Friendly Quantum-Dot-Based Photovoltaic Windows. *J. Mater. Chem. C* **2017**, *5*, 11790−11797.
(35) Allen, P. M.; Bawendi, M. G. Ternary I−III−VI Quantum Dots Luminescent in the Red to Near-Infrared. *J. Am. Chem. Soc.* **2008**, *130*, 9240−9241.
(36) McDaniel, H.; Koposov, A. Y.; Draguta, S.; Makarov, N. S.; Pietryga, J. M.; Klimov, V. I. Simple yet Versatile Synthesis of $CuInSe_xS_{2-x}$ Quantum Dots for Sunlight Harvesting. *J. Phys. Chem. C* **2014**, *118*, 16987−16994.
(37) Yarema, O.; Bozyigit, D.; Rousseau, I.; Nowack, L.; Yarema, M.; Heiss, W.; Wood, V. Highly Luminescent, Size- and Shape-Tunable Copper Indium Selenide Based Colloidal Nanocrystals. *Chem. Mater.* **2013**, *25*, 3753−3757.
(38) Castro, S. L.; Bailey, S. G.; Raffaelle, R. P.; Banger, K. K.; Hepp, A. F. Nanocrystalline Chalcopyrite Materials ($CuInS_2$ and $CuInSe_2$) via Low-Temperature Pyrolysis of Molecular Single-Source Precursors. *Chem. Mater.* **2003**, *15*, 3142−3147.
(39) Omata, T.; Nose, K.; Otsuka-Yao-Matsuo, S. Size Dependent Optical Band Gap of Ternary I-III-VI_2 Semiconductor Nanocrystals. *J. Appl. Phys.* **2009**, *105*, 073106.
(40) Yang, Y. H.; Chen, Y. T. Solvothermal Preparation and Spectroscopic Characterization of Copper Indium Diselenide Nanorods. *J. Phys. Chem. B* **2006**, *110*, 17370−17374.
(41) Koo, B.; Patel, R. N.; Korgel, B. A. Synthesis of $CuInSe_2$ Nanocrystals with Trigonal Pyramidal Shape. *J. Am. Chem. Soc.* **2009**, *131*, 3134−3135.
(42) Haizheng, Z.; Yunchao, L.; Mingfu, Y.; Zhongzheng, Z.; Yi, Z.; Chunhe, Y.; Yongfang, L. A Facile Route to Synthesize Chalcopyrite $CuInSe_2$ Nanocrystals in Non-Coordinating Solvent. *Nanotechnology* **2007**, *18*, 025602.
(43) Li, B.; Xie, Y.; Huang, J.; Qian, Y. Synthesis by a Solvothermal Route and Characterization of $CuInSe_2$ Nanowhiskers and Nanoparticles. *Adv. Mater.* **1999**, *11*, 1456−1459.

DOI: 10.1021/acs.chemmater.7b05187
Chem. Mater. 2018, 30, 2607−2617

(44) Saldanha, P. L.; Lesnyak, V.; Manna, L. Large Scale Syntheses of Colloidal Nanomaterials. *Nano Today* **2017**, *12*, 46−63.
(45) Nose, K.; Omata, T.; Otsuka-Yao-Matsuo, S. Colloidal Synthesis of Ternary Copper Indium Diselenide Quantum Dots and Their Optical Properties. *J. Phys. Chem. C* **2009**, *113*, 3455−3460.
(46) Akkerman, Q. A.; Genovese, A.; George, C.; Prato, M.; Moreels, I.; Casu, A.; Marras, S.; Curcio, A.; Scarpellini, A.; Pellegrino, T.; Manna, L.; Lesnyak, V. From Binary Cu_2S to Ternary Cu−In−S and Quaternary Cu−In−Zn−S Nanocrystals with Tunable Composition via Partial Cation Exchange. *ACS Nano* **2015**, *9*, 521−531.
(47) De Trizio, L.; Li, H.; Casu, A.; Genovese, A.; Sathya, A.; Messina, G. C.; Manna, L. Sn Cation Valency Dependence in Cation Exchange Reactions Involving $Cu_{2-x}Se$ Nanocrystals. *J. Am. Chem. Soc.* **2014**, *136*, 16277−16284.
(48) Lesnyak, V.; George, C.; Genovese, A.; Prato, M.; Casu, A.; Ayyappan, S.; Scarpellini, A.; Manna, L. Alloyed Copper Chalcogenide Nanoplatelets via Partial Cation Exchange Reactions. *ACS Nano* **2014**, *8*, 8407−8418.
(49) De Trizio, L.; Manna, L. Forging Colloidal Nanostructures via Cation Exchange Reactions. *Chem. Rev.* **2016**, *116*, 10852−10887.
(50) Park, J.; Kim, S.-W. $CuInS_2$/ZnS Core/Shell Quantum Dots by Cation Exchange and Their Blue-Shifted Photoluminescence. *J. Mater. Chem.* **2011**, *21*, 3745−3750.
(51) De Trizio, L.; Prato, M.; Genovese, A.; Casu, A.; Povia, M.; Simonutti, R.; Alcocer, M. J. P.; D'Andrea, C.; Tassone, F.; Manna, L. Strongly Fluorescent Quaternary Cu-In-Zn-S Nanocrystals Prepared from $Cu_{1-x}InS_2$ Nanocrystals by Partial Cation Exchange. *Chem. Mater.* **2012**, *24*, 2400−2406.
(52) van der Stam, W.; Bladt, E.; Rabouw, F. T.; Bals, S.; de Mello Donega, C. Near-Infrared Emitting $CuInSe_2$/$CuInS_2$ Dot Core/Rod Shell Heteronanorods by Sequential Cation Exchange. *ACS Nano* **2015**, *9*, 11430−11438.
(53) Lesnyak, V.; Brescia, R.; Messina, G. C.; Manna, L. Cu Vacancies Boost Cation Exchange Reactions in Copper Selenide Nanocrystals. *J. Am. Chem. Soc.* **2015**, *137*, 9315−9323.
(54) Liu, Y.; Yao, D.; Shen, L.; Zhang, H.; Zhang, X.; Yang, B. Alkylthiol-Enabled Se Powder Dissolution in Oleylamine at Room Temperature for the Phosphine-Free Synthesis of Copper-Based Quaternary Selenide Nanocrystals. *J. Am. Chem. Soc.* **2012**, *134*, 7207−7210.
(55) Hÿtch, M. J.; Snoeck, E.; Kilaas, R. Quantitative Measurement of Displacement and Strain Fields from HREM Micrographs. *Ultramicroscopy* **1998**, *74*, 131−146.
(56) Barkhouse, D. A. R.; Debnath, R.; Kramer, I. J.; Zhitomirsky, D.; Pattantyus-Abraham, A. G.; Levina, L.; Etgar, L.; Grätzel, M.; Sargent, E. H. Depleted Bulk Heterojunction Colloidal Quantum Dot Photovoltaics. *Adv. Mater.* **2011**, *23*, 3134−3138.
(57) Pearson, R. G. Absolute Electronegativity and Hardness: Application to Inorganic Chemistry. *Inorg. Chem.* **1988**, *27*, 734−740.
(58) Erwin Riedel, C. J. *Anorganische Chemie*; De Gruyter: 2011; Vol. *8*, p 979.
(59) Ishii, M.; Shibata, K.; Nozaki, H. Anion Distributions and Phase Transitions in $CuS_{1-x}Se_x$(x = 0−1) Studied by Raman Spectroscopy. *J. Solid State Chem.* **1993**, *105*, 504−511.
(60) Bacewicz, R.; Gebicki, W.; Filipowicz, J. Raman Scattering in $CuInS_{2x}Se_{2(1-x)}$ Mixed Crystals. *J. Phys.: Condens. Matter* **1994**, *6*, L777.
(61) Camus, C.; Rudigier, E.; Abou-Ras, D.; Allsop, N. A.; Unold, T.; Tomm, Y.; Schorr, S.; Gledhill, S. E.; Köhler, T.; Klaer, J.; Lux-Steiner, M. C.; Fischer, C.-H. Phonon Confinement and Strain in $CuInS_2$. *Appl. Phys. Lett.* **2008**, *92*, 101922.
(62) Dzhagan, V. M.; Litvinchuk, A. P.; Valakh, M. Y.; Kruszynska, M.; Kolny-Olesiak, J.; Himcinschi, C.; Zahn, D. R. T. Raman Scattering in Orthorhombic $CuInS_2$ Nanocrystals. *Phys. Status Solidi A* **2014**, *211*, 195−199.
(63) Li, J.; Kempken, B.; Dzhagan, V.; Zahn, D. R. T.; Grzelak, J.; Mackowski, S.; Parisi, J.; Kolny-Olesiak, J. Alloyed $CuInS_2$-ZnS Nanorods: Synthesis, Structure and Optical Properties. *CrystEngComm* **2015**, *17*, 5634−5643.
(64) Raevskaya, A.; Rosovik, O.; Kozytskiy, A.; Stroyuk, O.; Dzhagan, V.; Zahn, D. R. T. Non-Stoichiometric Cu-In-S@ZnS Nanoparticles Produced in Aqueous Solutions as Light Harvesters for Liquid-Junction Photoelectrochemical Solar Cells. *RSC Adv.* **2016**, *6*, 100145−100157.
(65) Dzhagan, V.; Kempken, B.; Valakh, M.; Parisi, J.; Kolny-Olesiak, J.; Zahn, D. R. T. Probing the Structure of $CuInS_2$-ZnS Core-Shell and Similar Nanocrystals by Raman Spectroscopy. *Appl. Surf. Sci.* **2017**, *395*, 24−28.
(66) Kriegel, I.; Scotognella, F.; Manna, L. Plasmonic Doped Semiconductor Nanocrystals: Properties, Fabrication, Applications and Perspectives. *Phys. Rep.* **2017**, *674*, 1−52.
(67) Dorfs, D.; Härtling, T.; Miszta, K.; Bigall, N. C.; Kim, M. R.; Genovese, A.; Falqui, A.; Povia, M.; Manna, L. Reversible Tunability of the Near-Infrared Valence Band Plasmon Resonance in $Cu_{2-x}Se$ Nanocrystals. *J. Am. Chem. Soc.* **2011**, *133*, 11175−11180.
(68) Llorente, V. B.; Dzhagan, V. M.; Gaponik, N.; Iglesias, R. A.; Zahn, D. R. T.; Lesnyak, V. Electrochemical Tuning of Localized Surface Plasmon Resonance in Copper Chalcogenide Nanocrystals. *J. Phys. Chem. C* **2017**, *121*, 18244−18253.
(69) Xie, R.; Rutherford, M.; Peng, X. Formation of High-Quality I−III−VI Semiconductor Nanocrystals by Tuning Relative Reactivity of Cationic Precursors. *J. Am. Chem. Soc.* **2009**, *131*, 5691−5697.
(70) Zhong, H.; Zhou, Y.; Ye, M.; He, Y.; Ye, J.; He, C.; Yang, C.; Li, Y. Controlled Synthesis and Optical Properties of Colloidal Ternary Chalcogenide $CuInS_2$ Nanocrystals. *Chem. Mater.* **2008**, *20*, 6434−6443.
(71) Slejko, E. A.; Sayevich, V.; Cai, B.; Gaponik, N.; Lughi, V.; Lesnyak, V.; Eychmüller, A. Precise Engineering of Nanocrystal Shells via Colloidal Atomic Layer Deposition. *Chem. Mater.* **2017**, *29*, 8111−8118.
(72) Debnath, T.; Maiti, S.; Maity, P.; Ghosh, H. N. Subpicosecond Exciton Dynamics and Biexcitonic Feature in Colloidal $CuInS_2$ Nanocrystals: Role of In−Cu Antisite Defects. *J. Phys. Chem. Lett.* **2015**, *6*, 3458−3465.
(73) Jara, D. H.; Yoon, S. J.; Stamplecoskie, K. G.; Kamat, P. V. Size-Dependent Photovoltaic Performance of $CuInS_2$ Quantum Dot-Sensitized Solar Cells. *Chem. Mater.* **2014**, *26*, 7221−7228.
(74) Fuhr, A. S.; Yun, H. J.; Makarov, N. S.; Li, H.; McDaniel, H.; Klimov, V. I. Light Emission Mechanisms in $CuInS_2$ Quantum Dots Evaluated by Spectral Electrochemistry. *ACS Photonics* **2017**, *4*, 2425−2435.
(75) Li, L.; Pandey, A.; Werder, D. J.; Khanal, B. P.; Pietryga, J. M.; Klimov, V. I. Efficient Synthesis of Highly Luminescent Copper Indium Sulfide-Based Core/Shell Nanocrystals with Surprisingly Long-Lived Emission. *J. Am. Chem. Soc.* **2011**, *133*, 1176−1179.
(76) Zang, H.; Li, H.; Makarov, N. S.; Velizhanin, K. A.; Wu, K.; Park, Y.-S.; Klimov, V. I. Thick-Shell $CuInS_2$/ZnS Quantum Dots with Suppressed "Blinking" and Narrow Single-Particle Emission Line Widths. *Nano Lett.* **2017**, *17*, 1787−1795.
(77) Pinchetti, V.; Lorenzon, M.; McDaniel, H.; Lorenzi, R.; Meinardi, F.; Klimov, V. I.; Brovelli, S. Spectro-electrochemical Probing of Intrinsic and Extrinsic Processes in Exciton Recombination in I−III−VI_2 Nanocrystals. *Nano Lett.* **2017**, *17*, 4508−4517.

DOI: 10.1021/acs.chemmater.7b05187
Chem. Mater. 2018, 30, 2607−2617